



Full length article

## Phosphorus driven embrittlement and atomistic crack behavior in tungsten grain boundaries

Praveenkumar Hiremath<sup>a,\*</sup>, Solveig Melin<sup>a</sup>, Pär A.T. Olsson<sup>a,b</sup><sup>a</sup> Division of Mechanics, Materials & Component Design, Lund University, Box 118, Lund, SE-221 00, Sweden<sup>b</sup> Materials Science and Applied Mathematics, Malmö University, SE-205 06 Malmö, Sweden

## ARTICLE INFO

## Keywords:

Tungsten

Phosphorus

Grain boundary embrittlement

Molecular statics

Fracture mechanisms

Cohesive zone volume elements

## ABSTRACT

We investigated the role of phosphorus (P) impurities on the fracture toughness and underlying failure mechanisms by means of classical atomistic modeling for a set of  $\langle 110 \rangle$  symmetric tilt tungsten grain boundaries (GBs). This entailed the utilization of a quasi-static mode I displacement-controlled setup with cohesive zone volume elements (CZVEs) to study failure mechanisms and evaluate the fracture toughness of the GB cracks. The fracture toughness was estimated using three approaches: computing (i) the individual and (ii) the average energy release rate of CZVEs along the fractured surfaces and using them as inputs for the Griffith model, and (iii) relating the fracture toughness to crack propagation initiation. The cracks in all the pristine GBs evolved in a brittle fashion, occasionally forming faceted cleavage planes. Upon introduction of impurities, other mechanisms such as void formation and crack-tip transformation were also observed. Depending on the GB proximity of the occupied segregation sites, local strengthening was seen occasionally for individual CZVEs and at the crack-tip, which was triggered by local impurity-induced crack deflection onto planes with higher cohesion. But when the fracture toughness from the averaged energy release rate was considered, an overall reduction with increasing impurity segregation was found, although to a varying degree for different GBs. This indicates an overall increased degree of embrittlement with increasing P-segregation at the GBs, which concurs with most experimental results reported in the literature.

## 1. Introduction

Plasma-facing components (PFCs) in nuclear fusion reactors such as ITER and DEMO need to function in an extreme environment where they are exposed to high thermal loads and intense neutron radiation. This necessitates that the PFCs are composed of high-performing materials that can sustain the harsh conditions of reactors. Owing to their high melting temperature, high thermal conductivity, low thermal expansion, high-temperature strength, and sputtering resistance [1–10], tungsten (W) and its alloys are the likely materials of choice for such applications. However, W-alloys exhibit a high brittle-to-ductile transition temperature (BDTT), which lies in an approximate range of 150–500 °C for polycrystals [11–14]. As a result, components such as the centrally cooled monoblocks that comprise the divertor may fail in a brittle fashion due to the induced thermal gradients [15,16]. The BDTT is significantly influenced by the microstructure, presence of impurities, and mobility of defects such as screw dislocations [17,18]. The microstructure is characterized by grains of different average diameters and grain boundaries (GBs), where the latter is of primary importance as intergranular fracture typically occurs at a lower resistance than

transgranular fracture in W. In addition, the ductility of materials is impacted by the cohesive strength of the GBs [19]. For instance, Reiser et al. [20] showed that when W is cold-rolled at sub-recrystallization temperature, the BDTT reduces as a result of an increased number of low-angle GBs that host dislocations, which indicates improved ductility.

Non-metallic impurities in polycrystalline W – even in trace amounts – tend to segregate to the GBs at which they can significantly alter the fracture properties. Impurities like carbon and boron have proven to be beneficial by improving the GB strength [21–23], whereas phosphorus (P), oxygen, and sulfur have deleterious effects as they induce further embrittlement of GBs by reducing their strength in polycrystals [21,24–26]. Specifically, P impurities are seen as major contributors to the embrittlement of GBs in technically pure W. They bring about a reduction in ductility, which generally promotes an increased amount of intergranular fracture with increasing P segregation [25–27]. However, the experimental fracture study conducted by Gludovatz et al. [28] reported that the GB impurity content plays an insignificant role in controlling the amount of trans- vs. intergranular

\* Corresponding author.

E-mail address: [praveenkumar.hiremath@mek.lth.se](mailto:praveenkumar.hiremath@mek.lth.se) (P. Hiremath).

fracture for specimens with P impurities up to 20 wppm. Instead, it was argued that the microstructural properties (grain size, shape, etc.) are more important for the fracture behavior [28], which could be indicative of P only inducing GB embrittlement above a certain impurity concentration threshold. This merits further investigation.

Besides experimental characterization, electronic methods like density functional theory (DFT) have also been used to investigate how P impurities affect GB cohesion. These simulations – sometimes also referred to as ideal work of separation ( $W_{sep}^{GB}$ ) calculations – can be rigid or relaxed and provide the GB decohesion energetics associated with the ideal energy release rate. Based on the correlation between  $W_{sep}^{GB}$  and the concentration of GB segregated P impurities, the latter's impact on the GB cohesion can be evaluated. A DFT study of the fracture behavior of a  $\Sigma 3(111)[\bar{1}\bar{1}0]$  symmetric-tilt (ST) GB by Scheiber et al. [29] showed that it was weakened due to P impurities. The same observations were evident in the works of Krasko et al. [30], Pan et al. [31], and Olsson and Blomqvist [5]. However, in contrast to these results, Setyawan and Kurtz [32] reported that P impurities in a  $\Sigma 27(552)[\bar{1}\bar{1}0]$  GB improved the GB cohesion. Such contradicting observations prompt further investigation of the influence of P impurities on the GB cohesion. Moreover, the fact that such simulations are constrained to prescribed crack planes is a limitation and do not reflect the actual crack growth scenario for GBs with impurities, since impurities may promote alternative crack paths. Hence, alternative approaches, which do not necessitate the specification of active crack planes on beforehand, are needed.

To the best of the authors' knowledge, the classical atomistic works on P-induced GB embrittlement in W are scarce. The atomistic study carried out by Grujicic et al. [33] using molecular dynamics (MD) modeling at 100 K, showed that the load at which cracks propagate in a  $\Sigma 3(111)[\bar{1}\bar{1}0]$  GB is lower in the presence of P atoms occupying trigonal interstitial sites. They also reported that the ideal work of separation is reduced. The notion of an embrittling effect of P impurities was also supported in [34], by performing room-temperature MD tensile simulations. Again, the conclusion was that P reduces the cohesive strength of  $\langle 110 \rangle$  STGBs, but like most other studies, this work provided the influence of P on GB strength and *not* fracture related properties, like the fracture toughness ( $K_{IC}$ ). Other notable works on GB cohesion were undertaken by McDowell et al. [35] and Yamakov et al. [36] in copper and aluminum GBs, respectively. McDowell et al. [35] probed the stress vs. separation profile of a GB interface, also recognized as a cohesive zone, under displacement controlled tensile MD simulations. To extract a cohesive zone model constitutive law in terms of stress-separation relationship in aluminum GBs, Yamakov et al. [36] adopted an alternative approach where they subdivided the GB region into cohesive zone volume elements (CZVEs). Along the same lines as Yamakov et al. [36], to elucidate the change in cohesive strength of nickel GBs containing hydrogen impurities, Barrows et al. [37] extracted local stress-separation data from CZVEs.

Unlike the aforementioned approaches, atomistic crack setups that rely on stress intensity factor ( $K$ ) controlled displacement fields exhibit stable crack growth. Although the initial crack plane needs to be specified, the crack path is not on beforehand constrained to remain on any crack plane, which ultimately enables the crack to deflect if energetically favorable, see e.g. [38,39]. Such crack setups also allow for plastic mechanisms, such as dislocation nucleation and twinning, to ensue, which enables a balanced competition between brittle and ductile mechanisms at the crack-tip. Under these conditions, the crack is free to propagate onto energetically favorable planes, regardless of its complexities. As a consequence, the effect of impurities on the fracture properties of GBs can be realized better using such atomistic simulations. This setup has been previously used to extract the crack growth resistance as a function of the mode I applied loading in the form of an  $R$ -curve [40], which relates mode I stress intensity factor,  $K_I$ , and the crack extension,  $\Delta a_{crack}$ . From the atomistic  $R$ -curves, the fracture toughness associated with onset of crack-propagation,  $K_{IC}^R$ ,

can be estimated and aspects such as lattice or bond trapping can be investigated. But  $K_{IC}^R$  is not necessarily unique and may not be equivalent to the actual fracture toughness that causes the crack to advance, mainly for three reasons. (i) The  $K_{IC}^R$  associated with crack propagation initiation in GBs is highly dependent on the initial crack-tip position because of the varying bond strength along the GB structural unit, and on the impurity distribution in the crack-tip proximity, which can be heterogeneous and may not be representative of the remaining GB. (ii) For an accurate estimate of the fracture toughness beyond crack-initiation – as the crack gradually advances – the displacements need to be recomputed with respect to the updated crack-tip location, which is difficult to achieve numerically. Especially when the crack front is not a straight line, which is often the case when the material contains randomly dispersed solute atoms. (iii) The  $K_{IC}^R$  measurement is based on the observations of crack-tip displacements under prescribed displacement-controlled loading, which in turn depends on  $K_I$  and bulk elastic properties. But the impurity-induced changes in the atomic bond strength and bond length across the interface are not necessarily captured when combining such loading with displacement criteria to extract  $K_{IC}^R$ . Instead, in the spirit of Barrows et al. [37], it would be more meaningful to compute how properties that relate to the cohesion of the interface (e.g. maximum forces, ultimate strength, energy release rate, etc.) change upon introduction of impurities. Consequently, the extraction of the fracture toughness needs to be approached differently.

The objective of the current work is to investigate the role of P impurities on the fracture toughness and propagation behavior for a set of  $\langle 110 \rangle$  STGBs. We utilize the aforementioned  $K_I$ -controlled displacement setup, in tandem with CZVEs, to load and then unload the crack for the purpose of extracting the local and average energy release rate associated with brittle growth. Since the energy release rate is directly connected to the GB cohesion – via the Griffith model [41] – it enables the assessment of the impact of impurities on the fracture toughness. In addition, we evaluate the threshold toughness,  $K_{IC}^R$ , by which the crack propagation initiation occurs, for all considered GBs and impurity concentrations to highlight the differences in results that can be obtained for the two approaches.

The paper is organized as follows: In the next section, methods for preparing ground state STGB geometries, with or without P impurities, and setups for fracture simulations are described. The results section comprises the outcomes of the GB crack fracture simulations. This is followed by a discussion on the role of P impurities in the observed fracture behavior of GB cracks and its impact on the fracture toughness. Finally, a summary of the work and conclusions drawn are provided.

## 2. Computational methods

The LAMMPS package [42,43] was used for all the atomistic simulations in this work. The interatomic interaction was represented by the second nearest neighbor modified embedded atom method (2NN-MEAM [44,45]) potential developed in [34]. To the best of the authors' knowledge, the only other W-P potential used for atomistic simulations can be found in the work of Grujicic et al. [33]. This potential was a Finnis–Sinclair (FS) [46] type of potential, which was expanded to include the interactions due to P impurities. However, because the potential in [34] reproduces GB energies ( $\gamma_{GB}$ ), surface energies ( $\gamma_s$ ) and the ideal work of separation ( $W_{sep}^{GB} = 2\gamma_s - \gamma_{GB}$ ) as predicted by DFT [18] very well (see Fig. 1), it was chosen over the FS potential in [33]. Further, important fracture properties like traction–separation behavior and stacking fault energetics for varying degrees of P impurity coverage are predicted by this W-P potential with close to DFT accuracy [34]. As such, the potential has shown the ability to reproduce the experimentally concluded tendencies of W GB embrittlement due to P impurities.



were generated in the form of a cylinder of radius  $\sim 150$  Å. The crack-tip was positioned at the center of the cylinder to coincide with the origin of the Cartesian coordinate system that defines the crack geometry, see Fig. 3. The  $x$ - and  $y$ -axes corresponded to the crack propagation and crack plane normal directions, respectively, while the initial crack front was aligned with the  $z$ -axis. In terms of boundary conditions, only the crack front direction was periodic, while the other boundaries had prescribed displacements based on the stress intensity factor-controlled anisotropic displacement fields under plane strain, see e.g. [58–60].

In the literature, there are two main geometrical crack setups that are frequently employed in atomistic modeling: (i) blunted crack, created by removing atomic layers behind the crack-tip ( $x < 0$ , see Fig. 3), and (ii) atomically sharp crack with screened interaction across the crack plane. In the present work, we opted to go with the latter, mainly because blunting can modify the crack-tip singularity and promote a simulated fracture toughness that is considerably higher than LEFM predictions, while results from atomically sharp cracks tend to be more in line with LEFM [39,61]. Thus, to effectively cancel the forces across the crack plane, the interactions between atoms in the upper and lower regions of the left half of the cylindrical GB geometry (i.e. atoms with  $x < 0$ , see Fig. 3) were removed and remained turned off throughout the simulation.

The anisotropic displacement field was incrementally applied to update the atomic positions, under hybrid stress border conditions (HSBC) [62]. In line with HSBC, an inner region of free atoms extending radially from the crack-tip, as shown in Fig. 3, with  $\sim 120$  Å radius and a contiguous boundary region of at least 30 Å thickness were selected. The latter is approximately five times the cutoff radius of the used 2NN-MEAM potential, which ensured that the effect of free boundaries was effectively canceled out. The cylinder thickness in the periodic  $z$ -direction was chosen to be  $\sim 40$  Å thick, see Fig. 3. The herein adopted dimensions of the GB geometries were chosen on the basis of a  $K_{IC}$  convergence study presented in [60]. When loading via the displacement field, the boundary atoms were rigidly displaced whereas the atoms belonging to the region inside the outer boundaries were relaxed. To this end, we used the conjugate gradient algorithm [63] as implemented in LAMMPS and a stress intensity factor increment corresponding to  $\delta K = 0.0125$  MPa  $m^{1/2}$ . Because the crack front of most impurity-inhabited GBs went from a straight to curved line as the crack progressed, the crack-tip position could not be uniquely identified during the simulation, which prevented updating of the origin of the displacement field as the crack propagated.

### 2.2.1. Evaluation of energy release rate

To monitor the energy release rate during crack growth, we introduced a cohesive zone at the interface between the two grains with an approximate width of  $\sim 70$  Å, see Fig. 3. It was divided into smaller CZVEs, which had either the same width as the GB structural unit, or multiples thereof if it was less than 5.8 Å (approximately the interatomic potential cutoff radius). Artificially screened interactions to create the crack can influence the measurement of energy release rate,  $G_I^{CZ}$ , in the first CZVE if it was located in immediate connection to the crack-tip. Therefore, to remove any artifacts in the measurement of  $G_I^{CZ}$  in individual CZVEs, the CZVEs were placed with the first at a distance of at least 5.8 Å ahead of the crack-tip up to a maximum 70 Å. Throughout the simulation, the total potential energy of all atoms in each CZVE was tracked for every loading and unloading step. But because the total energy includes the strain energy due to the bulk response [64–66], as illustrated in Fig. 4, it scales with the considered volume of the CZVE, which makes it sensitive to its height. Moreover, owing to the fact that the application of the  $K_I$ -controlled displacement field induces a heterogeneous stress state, the bulk strain energy contribution for CZVEs located at different positions from the crack-tip will vary. This makes it difficult to deconvolute the energy release rate associated with decohesion of the fractured surface,  $G_I^{CZ}$ , for different CZVEs. To overcome this hurdle – once the crack had

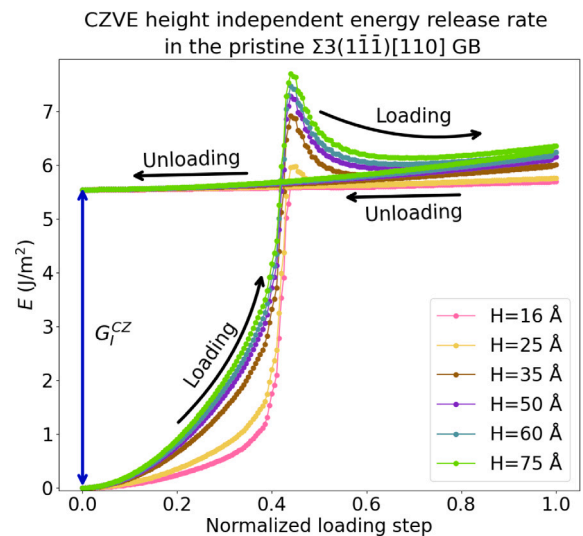


Fig. 4.  $E$  vs. normalized loading/unloading iteration curve for the pristine  $\Sigma 3(1\bar{1}\bar{1})$  GB with varying values of  $H$ . Here, the width of the CZVEs is 7.75 Å, which is equal to the width of the GB structural unit.

propagated for sufficiently long,  $\gtrsim 80$  Å – the interaction across the fractured surface was removed and the loading was reversed such that the prescribed boundary atoms could back-trace to re-assume the positions of the initially unloaded state. This way we could compute  $G_I^{CZ}$  associated with brittle failure as the energy difference between the initial and final states, as indicated in Fig. 4.

Owing to the fact that the prescribed  $K_I$ -controlled displacements are computed using the crack-tip location as a reference, ideally, the reference point for the displacements should be updated to follow the crack-tip as the crack advances. This is necessary to probe local variations of  $K_{IC}^R$  along the interface. However as illustrated in the Results section, in the case of studying the energy release rate, this turned out not to have any substantial impact on the results. Any variations in the energy release rate in individual CZVEs were small (at most  $\sim 2\%$  for the  $\Sigma 51$  GB crack) for those of pristine GBs placed within  $\sim 70$  Å of the original crack-tip, see Fig. 3.

This approach leads to a consistent reproduction of the ideal work of separation for most considered pristine GBs, with the maximum deviation being 8%. Thus, although the fracture surfaces were less ordered for impurity inhabited GBs, the outlined approach is applicable also to extract the energy release rate for non-pristine cases.

Once the  $G_I^{CZ}$ -values were determined, we computed the fracture toughness values of five consecutive CZVEs along the crack propagation direction using the Griffith model, i.e.,

$$K_{IC}^{CZ} = \sqrt{\frac{G_I^{CZ}}{B}} \quad (1)$$

where  $B$  is the anisotropic compliance constant [41,58–60]. Moreover, for both the energy release rate and the fracture toughness, we computed the average values, i.e.  $G_I$  and  $K_{IC}$ -values, of which the latter was computed as  $\sqrt{G_I/B}$ , to quantify the overall impact of P-impurities on the mechanical properties.

### 2.2.2. Crack-propagation initiation

To determine the applied stress-intensity factor by which the crack starts to propagate, it is necessary to trace the crack movement from the initial crack-tip position. To this end, we studied the crack elongation  $\Delta a_{crack}$  vs.  $K_I$ , which enables the identification of  $K_{IC}^R$  as the loading instance at which  $\Delta a_{crack}$  transitions from zero to a non-zero value. Such  $\Delta a_{crack}(K_I)$ -curves are henceforth referred to as  $R$ -curves. Unlike the aforementioned energy release rate approaches, which yield either the

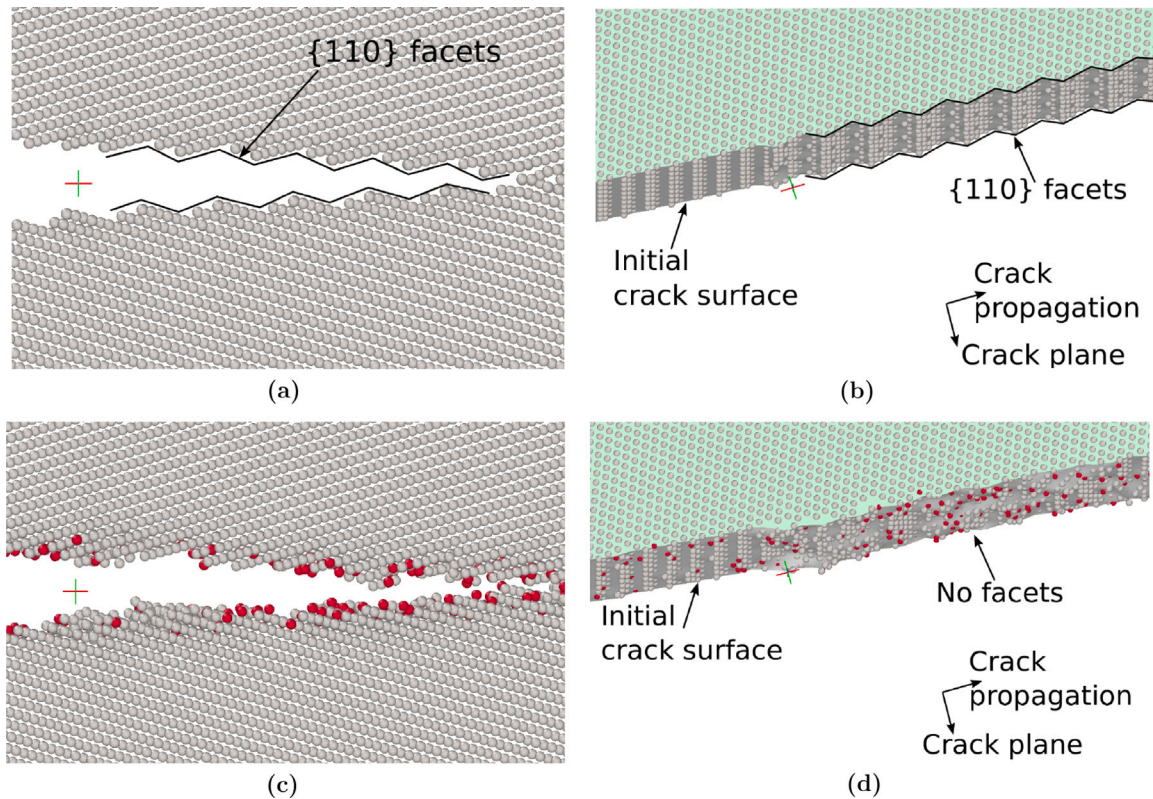


**Fig. 5.** Facetting in the pristine  $\Sigma 9$  GB (a) view along the crack-front and (b) upper half of the crack visualized using surface mesh construction. Lack of facetting in the P-impurity inhabited  $\Sigma 9$  GB (c) view along the crack-front and (d) upper half of the crack visualized using surface mesh construction. The gray and red colored atoms correspond to W and P atoms, respectively. The '+' sign represents the initial location of crack-tip before loading.

fracture toughness of individual CZVEs or an averaged assessment of the same for the GB as a whole, this provides a local fracture toughness estimate at the initial crack-tip.

Owing to the discrete nature, to monitor  $\Delta a_{crack}$  we utilized a two-step procedure. The first step in this approach involved the identification of all the atoms in the vicinity of the GB interface whose Voronoi volume [67] was considerably larger than that of bulk and GB interface atoms before loading. This was done using the Voro++ package [68]. Visual inspection of configurations using the OVITO software [69] showed that for most GBs, a threshold value of  $22 \text{ \AA}^3$  was sufficient to differentiate the low-coordinated atoms positioned either at the crack surfaces or crack-tip from the others. Accordingly, it was used as the threshold for all GBs, except the  $\Sigma 9$  GB, for which we found it necessary to use a higher threshold of  $26 \text{ \AA}^3$ . As a comparison, the ideal atomic volume of BCC W is  $15.85 \text{ \AA}^3$ , as predicted by the current potential, which indicates that the utilized threshold volumes are  $\sim 40\%$  larger than that of a perfect bulk atom. In the second step, the crack-tip position, and consequently  $\Delta a_{crack}$ , was estimated to be the maximum  $x$ -coordinate among the set of identified large-volume atoms. This enabled the identification of crack propagation initiation, even for cases when the crack front was curved.

### 3. Results

#### 3.1. Grain boundary structure and crack mechanisms

To gain insight into the dislocation structure of ground state configurations of the considered GBs, they were analyzed using the dislocation extraction algorithm (DXA) [70] implemented in the OVITO software. This revealed that the low angle (LA) GB  $\Sigma 51$  accommodates  $a\langle 100 \rangle$ -dislocations (where  $a$  is the lattice constant), while the high-angle (HA)  $\Sigma 33$  GB contain  $\frac{a}{2}\langle 111 \rangle$ -dislocations. For the remaining GBs, the algorithm could not identify any specific dislocation types.

The observed GB failure mechanisms are summarized in Table 2. Despite the occasional presence of dislocations, all the considered pristine GBs behave in a brittle manner, in accordance with the tensile modeling in [34]. Post-fracture analysis of the fracture surfaces using surface mesh construction based on the alpha shape algorithm [71], revealed that the propagation of almost half of the pristine GB cracks was associated with the formation of  $\{110\}$ -facets, see Fig. 5(a) and (b). They are referred to as  $B_{\{110\}}$  in the absence of dislocations. The  $\Sigma 51$  LAGB and  $\Sigma 33$  HAGB, which contain  $a\langle 100 \rangle$  and  $\frac{a}{2}\langle 111 \rangle$ -dislocations, respectively, underwent brittle failure whilst forming  $\{110\}$  facets. They are denoted as  $B_{\{110\}}^{(100)}$  and  $B_{\{110\}}^{(111)}$  in Table 2, respectively. For the remaining pristine GBs:  $\Sigma 3(\bar{1}12)$ ,  $\Sigma 11$ ,  $\Sigma 17(2\bar{2}\bar{3})$ ,  $\Sigma 17(3\bar{3}\bar{4})$ ,  $\Sigma 19$  and  $\Sigma 43$ , the cracks propagated in a brittle manner along the original GB plane without any facets forming.

Upon the introduction of P impurities, the GBs still underwent brittle propagation, but the facetting vanished, see Fig. 5(c) and (d). This rendered irregular crack surfaces decorated with P impurities. A coverage of  $\theta = 0.02 \text{ \AA}^{-2}$  was enough to suppress the formation of  $\{110\}$  facets completely in all the GBs. For two of the considered GBs,  $\Sigma 3(\bar{1}12)$  and  $\Sigma 51$ , other fracture mechanisms were observed. For the former (with  $\theta = 0.02 \text{ \AA}^{-2}$ ), the atoms ahead of the crack-tip formed a non-BCC structure, that was unidentifiable using the common neighbor analysis (CNA) algorithm [72]. Visual inspection of the local ordering indicated it to have random features, but since we were unable to classify it further we refer to it as crack-tip transformation, which is identified as  $B_{ctt}$  in Table 2. Such crack-tip transformation was never seen for any of the pristine GBs, see Fig. 6(a) and (b). For the  $\Sigma 51$  LAGB, impurities gave rise to the nucleation of voids, see Fig. 6(c) and (d). Such voids were not observed in any of the other GBs and is represented as  $B_{void}^{(100)}$  in Table 2.

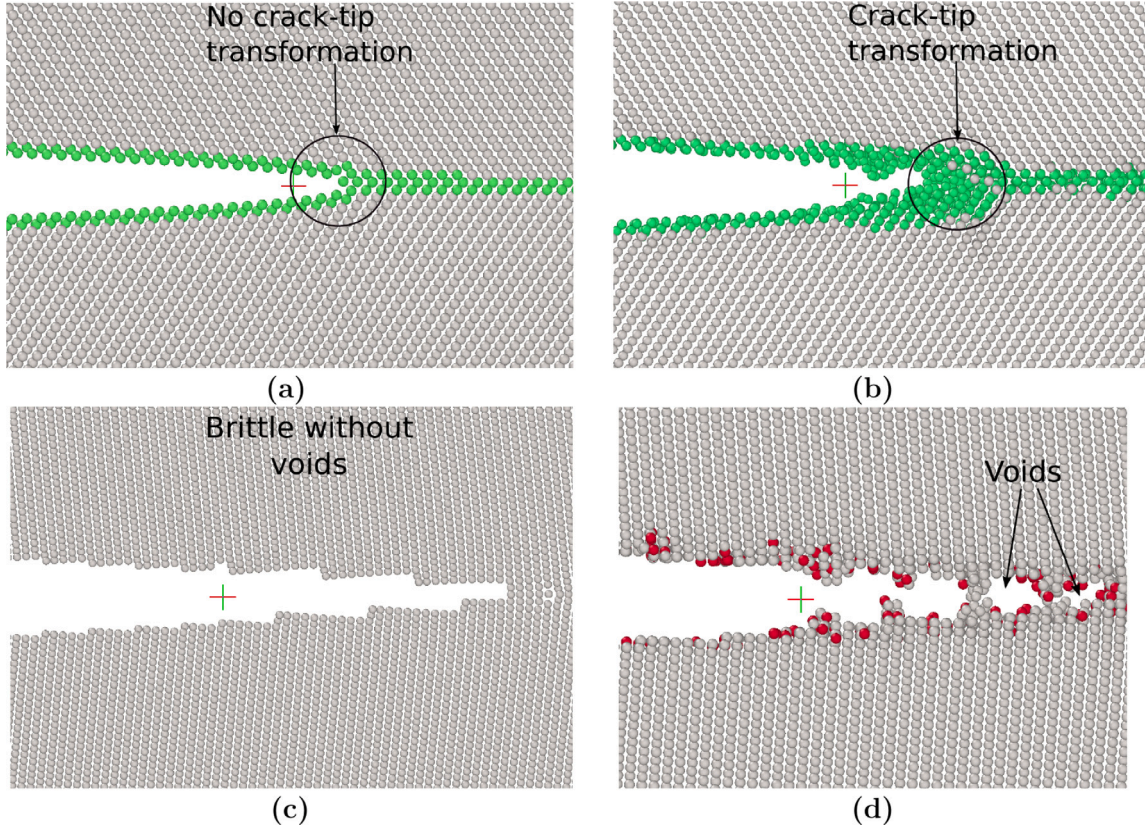


**Fig. 6.** (a, b) Illustration of crack-tip behavior for (a) the pristine  $\Sigma 3(\bar{1}12)$  GB and (b) that with the impurity coverage  $\theta = 0.04 \text{ \AA}^{-2}$  undergoing crack-tip transformation. The atomic coloring is based on a CNA analysis with gray and green atoms having BCC and unidentified structures, respectively. (c) Faceted brittle crack evolution in the pristine  $\Sigma 51$  GB and (d) void formation ahead of the crack-tip with impurity coverage  $\theta = 0.02 \text{ \AA}^{-2}$ , respectively. Here, gray and red atoms are W and P, respectively. The '+' sign is the initial location of crack-tip before loading.

**Table 2**

Crack mechanisms in  $\langle 110 \rangle$  STGBs considered in the present work. Here, 'pr.dir' is short for crack propagation direction, and  $\theta$  stands for P impurities coverage. B represents brittle failure. In the case of GBs with  $a\langle 100 \rangle$ - or  $a/2\langle 111 \rangle$ -type dislocations, the respective superscripts are used. Brittle failure with void formation in the GBs with  $a\langle 100 \rangle$ -type dislocations is referred to as  $B_{void}^{(100)}$ . Finally, when crack-tip transformation or facetting occurs, subscript 'ctt' or ' $\{110\}$ ' is used, respectively.

GB, crack system $\Sigma/\langle \text{pr.dir} \rangle$	$\theta = 0.0 \text{ \AA}^{-2}$	$\theta = 0.02 \text{ \AA}^{-2}$	$\theta = 0.04 \text{ \AA}^{-2}$	$\theta = 0.06 \text{ \AA}^{-2}$
$\Sigma 51/[55\bar{1}]$	$B_{(110)}^{(100)}$	$B_{(110)}^{(100)}$	$B_{void}^{(100)}$	$B_{void}^{(100)}$
$\Sigma 3(\bar{1}12)/[\bar{1}\bar{1}\bar{1}]$	B	$B_{ctt}$	$B_{ctt}$	$B_{ctt}$
$\Sigma 17(2\bar{2}\bar{3})/[\bar{3}\bar{3}\bar{4}]$	B	B	B	B
$\Sigma 17(3\bar{3}\bar{4})/[2\bar{2}\bar{3}]$	B	B	B	B
$\Sigma 43/[\bar{3}\bar{3}\bar{5}]$	B	B	B	B
$\Sigma 3(1\bar{1}\bar{1})/[1\bar{1}\bar{2}]$	$B_{(110)}$	B	B	B
$\Sigma 11/[2\bar{2}\bar{5}]$	B	B	B	B
$\Sigma 9/[1\bar{1}\bar{4}]$	$B_{(110)}$	B	B	B
$\Sigma 27/[1\bar{1}\bar{5}]$	$B_{(110)}$	B	B	B
$\Sigma 19/[1\bar{1}\bar{6}]$	B	B	B	B
$\Sigma 33/[\bar{1}\bar{1}\bar{8}]$	$B_{(110)}^{(111)}$	$B^{(111)}$	$B^{(111)}$	$B^{(111)}$

### 3.2. Energy release rate

To gain insight on the local variations of the energy release rate, we summarize the results from the evaluations of the individual CZVEs, see Fig. 7(a), along with the averaged values, see Fig. 7(b).

#### 3.2.1. Pristine grain boundaries

For the pristine GBs we find the  $G_I^{CZ}$ -values to be almost identical for all CZVEs, despite being located at different sites relative to the initial crack-tip position. The most significant variation is seen for the  $\Sigma 51$  GB. The observed variation of  $\sim 2\%$  relative to the averaged value

of the energy release rate demonstrates that the variation is indeed small and would translate to an uncertainty of only  $\sim 1\%$  in the computed  $K_{IC}$  based on the Griffith approximation. The fact that we obtain such uniform  $G_I^{CZ}$ -values for pristine GBs indicates that the parallel strain in the CZVEs along the crack plane due to the herein utilized displacement fields has a negligible effect on the extracted  $G_I^{CZ}$ -values. On comparison with the ideal  $W_{sep}^{GB}$ , it is noticed the  $G_I^{CZ}$  data concurs well. The most significant deviations were seen for the pristine  $\Sigma 9$ ,  $\Sigma 17(2\bar{2}\bar{3})$  and  $\Sigma 51$  GBs. The energy release rate overestimation in these GBs was  $\sim 5\text{--}8\%$  of which  $\Sigma 9$  showed the maximum deviation with respect to the corresponding  $W_{sep}^{GB}$ . These deviations are due to the fractured surfaces not being identical to the ideally cut crack planes that were used for the computation of the ideal  $W_{sep}^{GB}$ . These results indicate that the loading-unloading approach has the capability to extract a size-independent measure of the energy release rate, which is independent of the location of individual CZVEs.

#### 3.2.2. Impact of impurity segregation

Unlike the pristine GBs, upon introduction of P impurities, we find that the extracted  $G_I^{CZ}$  differs significantly for different CZVEs. Although P led to reduced  $G_I^{CZ}$  in the majority of the GBs, deviations from this behavior were also found. For instance, increased  $G_I^{CZ}$  was found for the  $\Sigma 3(\bar{1}12)$  GB, see Fig. 7(a). This is the result of crack-tip transformation, see Fig. 6(b), which is known to yield an increased fracture toughness, see e.g. [40,60].

More interestingly, for a subset of the considered GBs ( $\Sigma 11$ ,  $\Sigma 19$ ,  $\Sigma 27$ ,  $\Sigma 33$  and  $\Sigma 51$  GBs with  $\theta = 0.02 \text{ \AA}^{-2}$ ), of which all underwent brittle failure, the energy release rate was found to be higher for individual CZVEs following impurity segregation. This is due to impurities locally deflecting the crack onto planes with higher energy release rate,

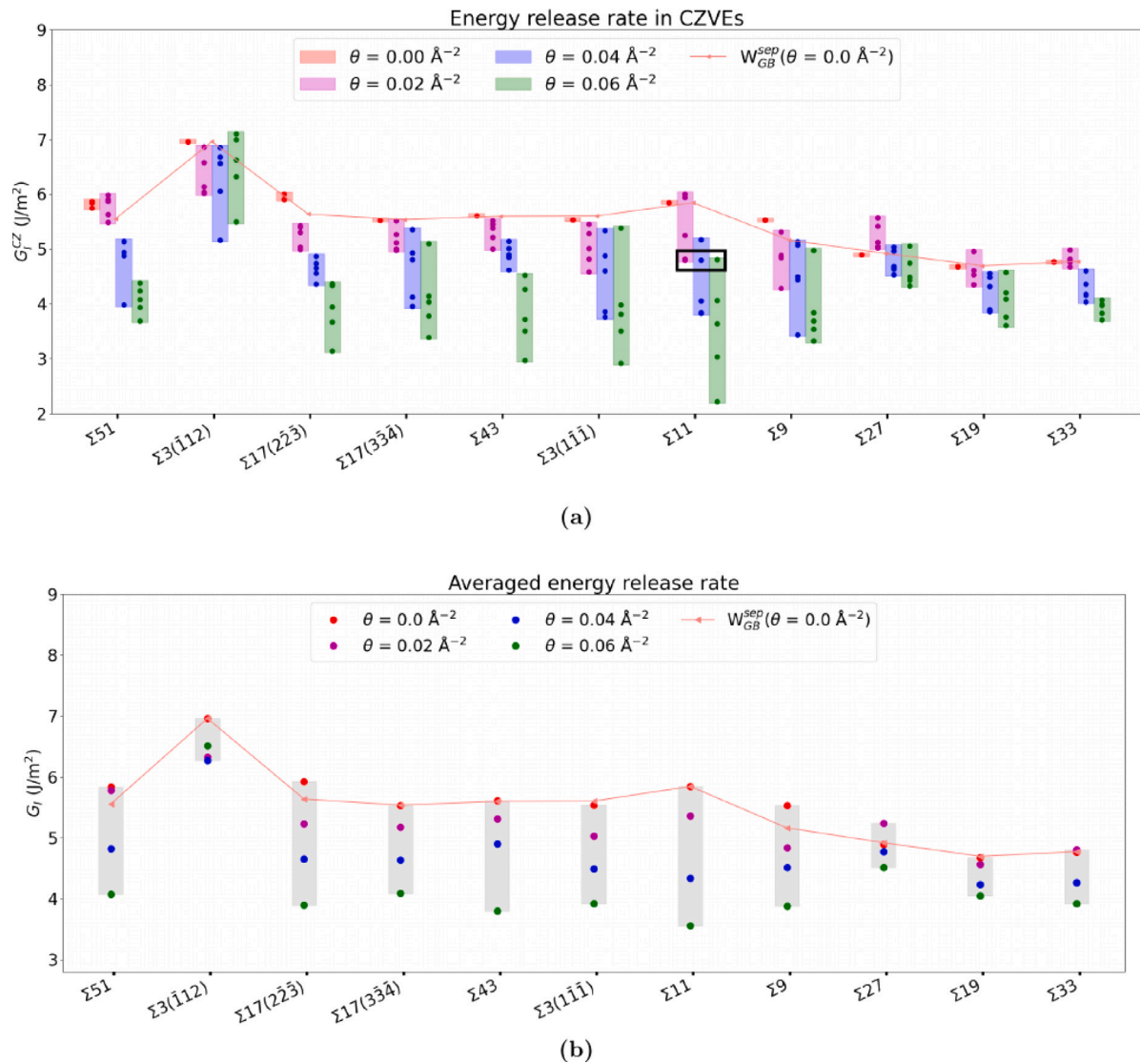


Fig. 7. (a) Energy release rate of individual CZVEs and (b) averaged energy release rate for all the GBs considered in the present work. In (a) the markers show the individual data associated with each considered CZVE, while the bars represent the range between the largest and smallest values. The encircled  $G_I^{CZ}$  values of the  $\Sigma 11$  GB in (a) represent the energy release rate for three CZVEs with varying impurity coverage, with results depicted in Fig. 8.

see e.g. Fig. 5(d). For such events to occur, not only do local variations in the P-impurity coverage between the CZVEs play an important role, but also the occupied segregation sites, which influence the local response and the crack propagation path. The fact that these local factors have a decisive impact on the response is further highlighted by close examination of three CZVEs for the  $\Sigma 11$  GB (encircled with a black rectangle in Fig. 7(a)). They are of special interest because they exhibit almost identical  $G_I^{CZ}$ , despite belonging to GBs with different average impurity coverage. For this particular case, it was found that the three CZVEs had the same number of impurities in the immediate proximity of the crack plane, see Fig. 8(a)–(c), while the remaining impurities occupied sites further away. As a result, not only are the local crack surfaces similar, see Fig. 8(d)–(f), but also the values of  $G_I^{CZ}$  are found to overlap.

By averaging the  $G_I^{CZ}$ -values from Fig. 7(a) we get  $G_I$ . The  $G_I$ -values for all the considered GB cracks are provided in Table S1 of the supplementary material and in Fig. 7(b). Overall, the impact of P impurities on the averaged energy release rate is similar to that on  $G_I^{CZ}$  in that  $G_I$  monotonically decreases as the P-coverage increases for most GBs. But the amount of reduction varies from one GB to another, as some GBs exhibit a more pronounced  $G_I$  reduction than others for the

same P impurity coverage. For example, an unusually large reduction was seen for the  $\Sigma 11$  GB, corresponding to  $\sim 64\%$ , whereas it was only  $\sim 15\%$  for the  $\Sigma 19$  GB when increasing the coverage from  $\theta = 0$  to  $0.06 \text{ \AA}^{-2}$ , see Fig. 7(b).

The only exception to monotonically decreasing behavior is found for the  $\Sigma 27$  GB, where  $G_I$  is higher in the case of  $\theta = 0.02 \text{ \AA}^{-2}$  than for the pristine GB. This is in line with the DFT study conducted in [32], but in contrast to the results in our previous finite-temperature MD tensile study where the strain energy and peak stress for this specific GB clearly reduced with increasing impurity coverage [34]. Although the increase is only small ( $0.34 \text{ J/m}^2$ , i.e. less than 7%), this is an indication that the impurity-induced disruption of the low energy facets in favor of a less regular fracture surface can locally lead to enhanced – or at least unaltered – energy release rate. Increasing the impurity coverage up to  $\theta = 0.06 \text{ \AA}^{-2}$  leads to an overall decrease in the energy release rate, but it is emphasized that the reduction is generally small for this GB. Although we have not investigated it further, it is likely that an even higher impurity coverage would further reduce  $G_I$ , see Fig. 7(b).

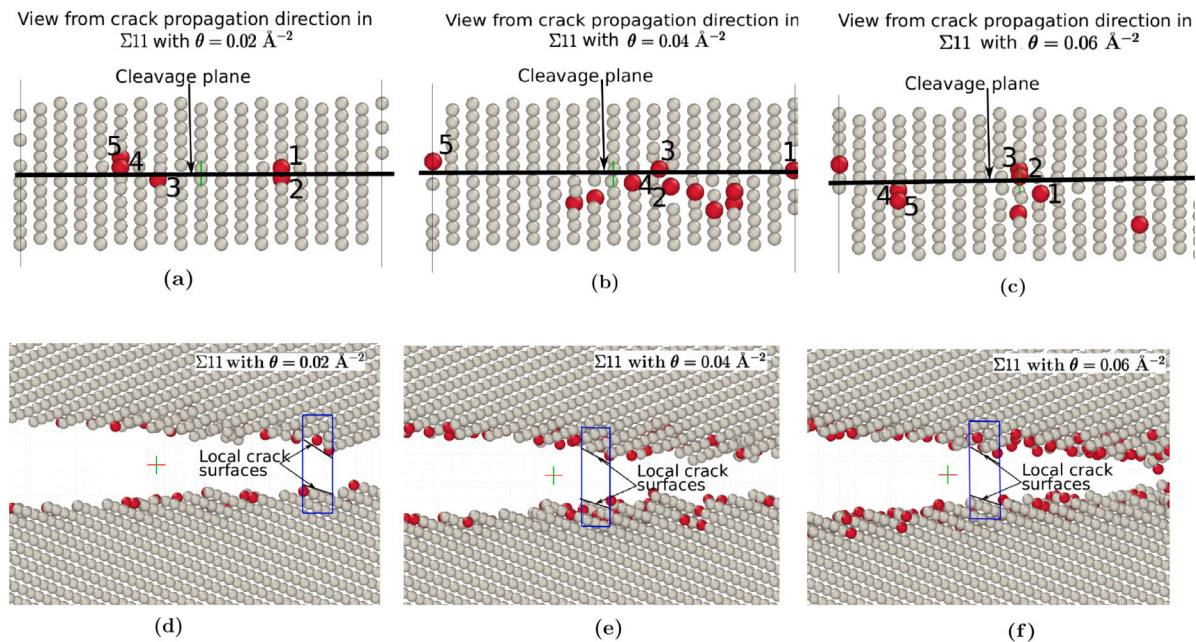


**Fig. 8.** The occupied P impurity segregation sites in the CZVEs, corresponding to the data points highlighted in Fig. 7(a), of  $\Sigma 11$  GB with (a)  $\theta = 0.02 \text{ \AA}^{-2}$ , (b)  $\theta = 0.04 \text{ \AA}^{-2}$  and (c)  $\theta = 0.06 \text{ \AA}^{-2}$ . Here, the black line indicates the cleavage plane as viewed from the crack propagation direction, and the atoms closest to the cleavage plane ( $\sim 1.5 \text{ \AA}$  from the plane) are numbered. The location of the CZVEs (as blue rectangles) relative to the initial crack-tip and the associated local crack surfaces are shown in (d)–(f).

### 3.3. Fracture toughness

To assess the impact of impurities on the fracture toughness, we compare the results obtained from the Griffith approximation and the  $R$ -curves. Most of the data is summarized in Fig. 9, with the resulting  $R$ -curves presented in their entirety in Figure S1–S2 of the supplementary material.

#### 3.3.1. Pristine grain boundaries

The local fracture toughness associated with individual CZVEs, i.e.  $K_{IC}^{CZ}$ -values, computed from  $G_I^{CZ}$ -values via Eq. (1), and  $K_{IC}^R$  extracted from the  $R$ -curves are compared in Fig. 9(a). Because there is very little variation in the  $G_I^{CZ}$ -data in the pristine state, the resulting  $K_{IC}^{CZ}$ -values do not display any significant variation. Compared with  $K_{IC}^R$  from the  $R$ -curves, it is found that the latter is mostly underestimated, but common for both approaches is that the twin boundary, i.e. the  $\Sigma 3(\bar{1}12)$  GB, is found to be the toughest. This is in agreement with LEFM predictions, as  $W_{sep}^{GB}$  is the highest among the considered GBs (see Fig. 1).

A comparison of the calculated  $K_{IC}^R$ -values for the  $\Sigma 3(\bar{1}\bar{1}\bar{1})$ ,  $\Sigma 3(\bar{1}\bar{1}2)$  and  $\Sigma 17(\bar{2}\bar{2}\bar{3})$  GBs with those previously reported in [60] reveals some discrepancy. Although no general trend can be delineated between the data herein and in [60], they differ by up to 27%, despite that the same interatomic potential was used. The most probable explanation for the observed discrepancy is the fact that  $K_{IC}^R$  is highly dependent on the location of the crack-tip prior to loading, since the strength of the atomic bonds and bond trapping varies along a GB structural unit. Moreover, such local variations give rise to a crack propagation-direction dependence, which may influence the extracted  $K_{IC}^R$ -values, see e.g. [38].

#### 3.3.2. Impurity-inhabited grain boundaries

In the presence of P impurities,  $K_{IC}^{CZ}$  is generally lower than that for the pristine GB cracks. However, the aforementioned variations in  $G_I^{CZ}$  lead to exceptions to this behavior for the  $\Sigma 11$ ,  $\Sigma 19$ ,  $\Sigma 27$ ,  $\Sigma 33$  and  $\Sigma 51$  GBs. Consequently, they occasionally yielded higher  $K_{IC}^{CZ}$ -values than in the corresponding pristine GB cracks, see Fig. 9(a).

Extraction of data from the  $R$ -curves, reveals reduction of  $K_{IC}^R$  for most GBs, which supports the notion that P segregation weakens

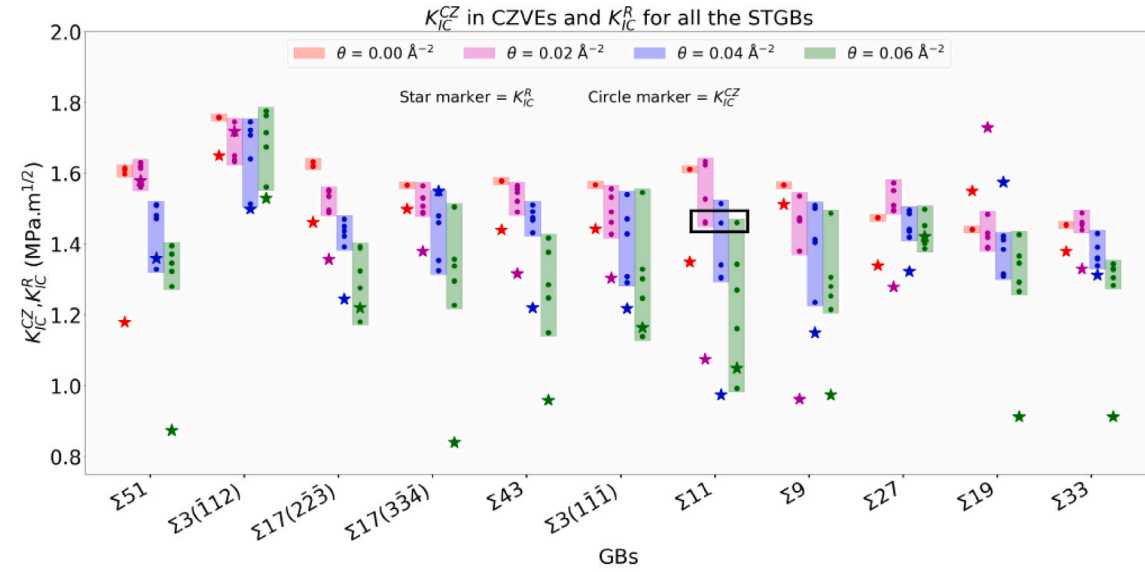
the atomic bonds ahead of the crack-tip. But again there are some exceptions to this behavior (e.g.  $\Sigma 51$ ,  $\Sigma 3(\bar{1}\bar{1}2)$ ,  $\Sigma 17(\bar{3}\bar{3}\bar{4})$ ,  $\Sigma 19$  and  $\Sigma 27$  GBs), for which  $K_{IC}^R$  is found to be higher in the presence of P impurities than in their absence, see Fig. 9. Moreover, for several of the considered GBs,  $K_{IC}^R$  is found to not decrease monotonically with gradually increasing impurity coverage. These tendencies indicate that the GB crack advancement is slower than in the corresponding pristine GB, which would imply a local strengthening. In line with the previously discussed variations in  $G_I^{CZ}$  and  $K_{IC}^{CZ}$ , this is a consequence of  $K_{IC}^R$  being a measure of the local behavior at the crack-tip where impurity-induced crack deflection, or in the case of the  $\Sigma 3(\bar{1}\bar{1}2)$  GB, crack-tip transformation in the immediate vicinity of the crack-tip may ensue.

To probe this further, for the  $\Sigma 11$  GB we mapped  $K_{IC}^R$  and  $K_{IC}^{CZ}$  against the resulting local coverage at the crack-tip and the considered CZVEs, see Fig. 10. For this GB, it is seen that if local variations in the impurity coverage are taken into account, an overall decreasing trend can be seen for both  $K_{IC}^{CZ}$  and  $K_{IC}^R$ . However, upon inspection of the same types of maps for the other herein considered GB (available in Figure S3–S12 in the supplementary material), this trend was generally not recovered. Also, the fact that several CZVEs (the markers highlighted in Fig. 10 by the encircling rectangles  $R_1$ – $R_2$ ) exhibited either the same impurity coverage and different  $K_{IC}^{CZ}$  or vice versa, emphasizes that the proximity of occupied segregation sites to the crack plane is important.

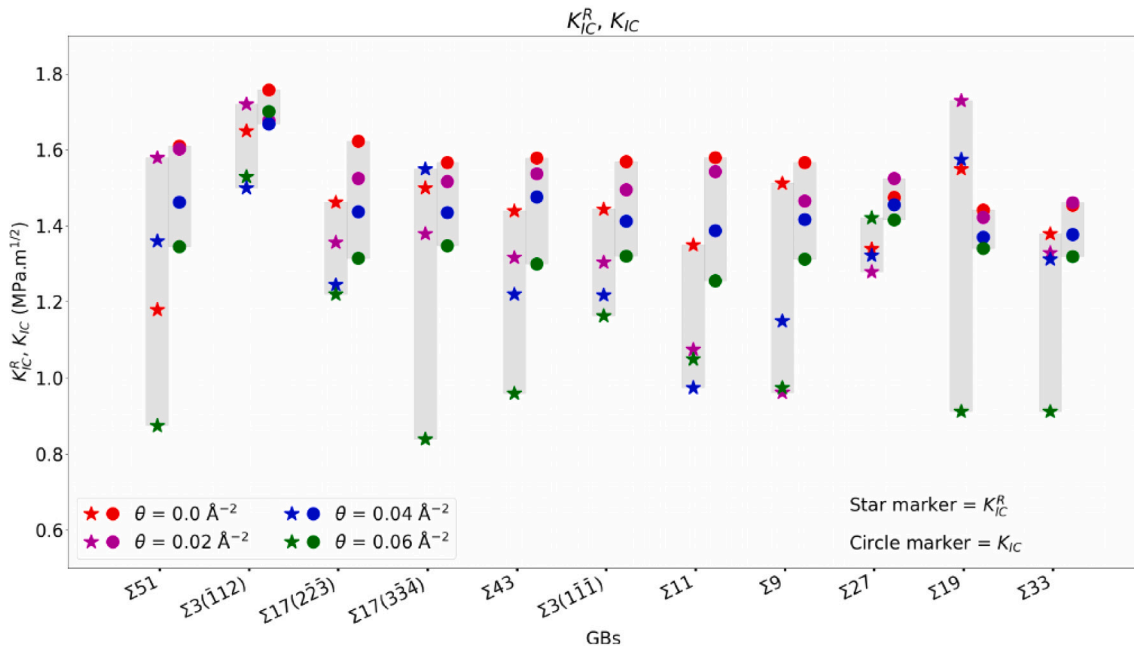
Despite the local variations of  $K_{IC}^{CZ}$  and  $K_{IC}^R$ , with the exception of the  $\Sigma 27$  GB, a monotonic decrease in the averaged fracture toughness,  $K_{IC}$ , with increasing impurity coverage is observed, see Fig. 9(b).

## 4. Discussion

For the cracks in the herein considered STGBs, only cleavage occurred, even for GBs that contained dislocations. Although the concentration of P impurities is low, they do impact the crack behavior in GBs. The  $\{110\}$  facets observed in some of the pristine GBs are suppressed by the P impurities that facilitate alternative minimum energy paths for crack propagation to ensue. This can have a local strengthening effect, as it may locally force the crack to redirect and propagate onto crack planes that are characterized by high  $W_{sep}^{GB}$  and only contain



(a)



(b)

Fig. 9. (a)  $K_{IC}^{CZ}$ -values in CZVEs and  $K_{IC}^R$ -values of all the GB cracks with varying impurity coverage,  $\theta$ . Here,  $K_{IC}^R$ -values are measured for  $\theta$  in the region ahead of the pre-loading crack tip and the first CZVE. The highlighted data points of the  $\Sigma 11$  GB in (a), correspond to the  $K_{IC}^{CZ}$ -values of the CZVEs marked in Fig. 8(d)–(f). (b)  $K_{IC}^R$  and  $K_{IC}$  values for varying  $\theta$  in the considered GBs. The data for these plots are provided in the supplementary material, see Tables S2 and S3 therein.

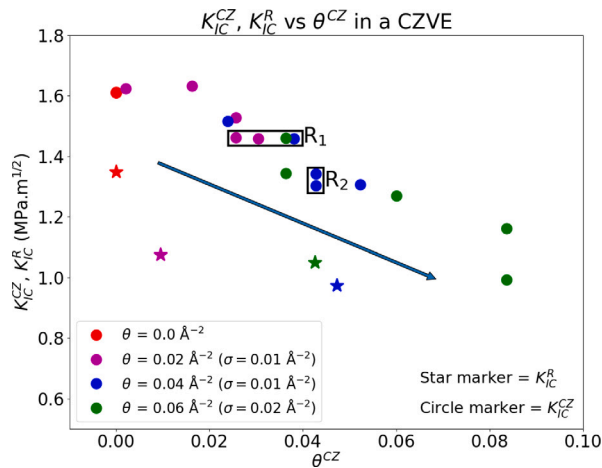


**Fig. 10.**  $K_{IC}^{CZ}$ -values in CZVEs of  $\Sigma 11$  GB cracks corresponding to the impurity coverage,  $\theta^{CZ}$ , in the CZVEs. Here,  $\sigma$  is the standard deviation of the P distribution among all the CZVEs of a GB. The arrow represents the overall decreasing trend in  $K_{IC}^{CZ}$  and  $K_{IC}^R$  with increasing  $\theta^{CZ}$ . Individual data points deviating from the trend are accentuated using rectangles  $R_1 - R_2$ . Similar plots for all the remaining GBs are provided in Figures S3–S12 of the supplementary material.

low impurity concentrations. The impurities can also lead to crack-tip transformation or void formation ahead of the crack-tip. For example, crack-tip transformation took place for the  $\Sigma 3(\bar{1}12)$  GB, where  $G_I^{CZ}$  associated with individual CZVEs is observed to be higher than the corresponding values in pristine GBs.

Any local variations of the energy release rate translate to the local fracture toughness  $K_{IC}^{CZ}$  via Eq. (1). However, as expected, the local absolute impurity coverage of a CZVE does not dictate its behavior alone, as also the proximity of the occupied segregation sites relative to the crack plane is of importance. This was shown for the  $\Sigma 11$  GB, where three CZVEs with different coverage, but the same number of impurities in immediate GB proximity, gave very similar energy release rate and fracture toughness.

Despite variation in the energy release rate of individual CZVEs, we find that on average it is mostly reduced by P impurities. Thus, ultimately  $G_I$  decreases with the increasing P impurity coverage. This follows from the impurities acting as screening ions across the GB interface [5], which leads to it becoming weaker when P impurities are segregated. As a result,  $K_{IC}$  is also reduced by the increasing  $\theta$ . A notable exception to this behavior is the  $\Sigma 27$  GB, for which the energy release rate increased marginally upon the introduction of impurities corresponding to the coverage of  $\theta = 0.02 \text{ \AA}^{-2}$ , while it decreased slightly upon further segregation of impurities. These findings concur with the results from a DFT investigation [49], where it was found that P segregation improves the cohesion of this particular GB. These results suggest that certain GBs have intrinsically higher resistance against embrittlement. Even though the intrinsic features that would lead to such enhancement are presently unknown, we note that also the  $\Sigma 3(\bar{1}12)$ ,  $\Sigma 19$  and  $\Sigma 33$  GBs are found to be only mildly affected by impurity segregation than the remaining GBs, see Fig. 7(b). It further supports the notion that there is a lower impurity segregation concentration below which embrittlement is negligible, as alluded by comparing results from previous experimental works in the literature [25,27,28]. However, this effect would be GB specific.

Because the bond strength varies along the GB structural unit,  $K_{IC}^R$ , which is measured exactly at the initial crack-tip, is highly sensitive to the location. Therefore, the found underestimation of  $K_{IC}^R$  in comparison with  $K_{IC}^{CZ}$  is likely an effect of breaking weaker bonds in the GB unit. For P-inhabited GBs, local variations in the impurity coverage and accompanying crack deflection are local factors that also impact  $K_{IC}^R$  and, analogous to  $G_I^{CZ}$ , may produce local strengthening. However,

the  $K_{IC}$  computed from  $G_I$  provides a more consistent estimate of the fracture toughness of impurity segregated GB cracks and its tendencies, and predicts behaviors that are in line with most published DFT works in the literature [5,29–31] and experiments [21,25–27]. The calculated  $G_I$  is the average behavior of a crack propagating through the CZVEs and does not just consider the crack-tip position, but also the P impurity segregation along the entire fractured surface. Thus, unlike the  $R$ -curve approach, which is highly dependent on local crack-tip morphology, impurity distribution and associated phenomena such as bond-trapping, the CZVE approach offers means to quantify the averaged reduction in cohesion. Owing to the fact that it relies on the energy release rate – and *not* crack-tip displacements – to assess the fracture toughness, it provides a less biased connection between the external load and material response such that chemically and geometrically-induced embrittling mechanisms and their interplay can be properly accounted for.

## 5. Summary and conclusions

In the present work, we have conducted a classical atomistic investigation of the GB embrittlement of W due to P impurities. To this end, we have implemented an approach based on CZVEs in tandem with quasi-static MS modeling to simulate stable crack-propagation. This was used to extract the energy release rate and to identify the crack-propagation initiation-load of GBs to estimate the fracture toughness. Among the benefits of using such approaches over conventional DFT GB traction–separation schemes is that the crack is not restricted to any prescribed crack-plane rather allowed to propagate on energetically preferential crack planes. Moreover, it has the advantage that it produces a stable crack propagation, which enables continuous evaluation of the energy release rate along the GB.

All the considered GB cracks were observed to undergo brittle failure, with additional features like facets, and upon impurity introduction, voids and crack-tip transformation in some cases. From the crack simulations, local energy release rate and fracture toughness were also extracted in individual CZVEs to better understand the influence of therein P distribution on the quantities. The  $G_I^{CZ}$  and  $K_{IC}^{CZ}$  are sensitive to the local impurity coverage and their segregation sites, along with events such as crack-tip transformation during crack growth. As anticipated, P impurities closest to a crack plane are the major contributors to the reduction in the energy release rate of P segregated GBs, as shown for  $\Sigma 11$  GB. The average energy release rate – and thereby  $K_{IC}$  – were found to consistently decrease with increasing impurity coverage, except for one GB: the  $\Sigma 27$  GB. This along with a few other GBs exhibited a lesser reduction in the energy release rate than the majority, which highlights that the impact of impurities on the ductility is GB specific.

When extracting  $K_{IC}^R$  from the  $R$ -curves, clear trends could not be delineated since  $K_{IC}^R$  increased with increasing P impurity coverage for a few GBs. Such deviant behavior is attributed to the occurrence of localized strengthening due to heterogeneous impurity segregation, crack-tip transformation, and morphology locally at the crack-tip. These localized effects were found to not have any significant impact on the overall cohesion of impurity-inhabited GBs, which is by most accounts reduced by P segregation. Thus, in line with most available experimental investigations, the results herein indicate that the fracture toughness of the GBs is generally lowered, albeit to a varying degree for different GBs, which supports the notion of an embrittling effect of P impurities in the GBs of W.

## CRedit authorship contribution statement

**Praveenkumar Hiremath:** Conceptualization, Methodology, Investigation, Formal analysis, Writing – original draft, review & editing. **Solveig Melin:** Writing – review & editing, Supervision, Funding acquisition. **Pär A.T. Olsson:** Conceptualization, Methodology, Writing – review & editing, Supervision, Funding acquisition.

## Declaration of competing interest

The authors declare that they have no known competing financial interests or personal relationships that could have appeared to influence the work reported in this paper.

## Data availability

The data required to reproduce these findings is available in the supplementary material.

## Acknowledgments

The authors gratefully acknowledge funding from the Swedish Research Council through grants no. 2016-04162, 2018-04348 and 2022-04497. The computations were enabled by resources provided by the National Academic Infrastructure for Supercomputing in Sweden (NAISS) at the National Supercomputer Centre (NSC), Linköping University.

## Appendix A. Supplementary data

Supplementary material related to this article can be found online at <https://doi.org/10.1016/j.commatsci.2024.113194>.

## References

- [1] S.J. Zinkle, Fusion materials science: Overview of challenges and recent progress, *Phys. Plasmas* 12 (5) (2005) 058101.
- [2] S. Matsuda, K. Tobita, Evolution of the ITER program and prospect for the next-step fusion DEMO reactors: status of the fusion energy R&D as ultimate source of energy, *J. Nucl. Sci. Technol.* 50 (4) (2013) 321–345.
- [3] G. Federici, A. Zhitlukhin, N. Arkhipov, R. Giniyatulin, N. Klimov, I. Landman, V. Podkovyrov, V. Safronov, A. Loarte, M. Merola, Effects of ELMs and disruptions on ITER divertor armour materials, *J. Nucl. Mater.* 337–339 (2005) 684–690.
- [4] J. Pamela, A. Bécoulet, D. Borba, J.L. Boutard, L. Horton, D. Maisonnier, Efficiency and availability driven R&D issues for DEMO, *Fusion Eng. Des.* 84 (2–6) (2009) 194–204.
- [5] P.A.T. Olsson, J. Blomqvist, Intergranular fracture of tungsten containing phosphorus impurities: A first principles investigation, *Comput. Mater. Sci.* 139 (2017) 368–378.
- [6] M. Rieth, J.L. Boutard, S.L. Dudarev, T. Ahlgren, S. Antusch, N. Baluc, M.F. Barthe, C.S. Becquart, L. Ciupinski, J.B. Correia, et al., Review on the EFDA programme on tungsten materials technology and science, *J. Nucl. Mater.* 417 (1–3) (2011) 463–467.
- [7] M. Rieth, S.L. Dudarev, S.G. De Vicente, J. Aktaa, T. Ahlgren, S. Antusch, D.E.J. Armstrong, M. Balden, N. Baluc, M.F. Barthe, et al., A brief summary of the progress on the EFDA tungsten materials program, *J. Nucl. Mater.* 442 (1–3) (2013) S173–S180.
- [8] H. Bolt, V. Barabash, G. Federici, J. Linke, A. Loarte, J. Roth, K. Sato, Plasma facing and high heat flux materials—needs for ITER and beyond, *J. Nucl. Mater.* 307 (2002) 43–52.
- [9] P. Norajitra, S.I. Abdel-Khalik, L.M. Giancarli, T. Ihli, G. Janeschitz, S. Malang, I.V. Mazul, P. Sardain, Divertor conceptual designs for a fusion power plant, *Fusion Eng. Des.* 83 (7–9) (2008) 893–902.
- [10] D. Maisonnier, D. Campbell, I. Cook, L. Di Pace, L. Giancarli, J. Hayward, A.L. Puma, M. Medrano, P. Norajitra, M. Roccella, et al., Power plant conceptual studies in Europe, *Nucl. Fusion* 47 (11) (2007) 1524.
- [11] V. Philipps, Tungsten as material for plasma-facing components in fusion devices, *J. Nucl. Mater.* 415 (1) (2011) S2–S9.
- [12] L. Gharraee, First Principles Study of Tungsten-Based Alloys: from Defect Thermodynamics to Phase Diagrams (Ph.D. thesis), Department of Chemistry and Chemical Engineering, Chalmers University of Technology, 2017.
- [13] M. Wirtz, I. Uytendhouben, V. Barabash, F. Escourbiac, T. Hirai, J. Linke, T. Loewenhoff, S. Panayotis, G. Pintsuk, Material properties and their influence on the behaviour of tungsten as plasma facing material, *Nucl. Fusion* 57 (6) (2017) 066018.
- [14] B.G. Butler, J.D. Paramore, J.P. Ligda, C. Ren, Z.Z. Fang, S.C. Middlemas, K.J. Hemker, Mechanisms of deformation and ductility in tungsten – A review, *Int. J. Refract. Met. Hard Mater.* 75 (2018) 248–261.
- [15] Y. Huang, M. Tillack, N. Ghoniem, Tungsten monoblock concepts for the fusion nuclear science facility (FNSF) first wall and divertor, *Fusion Eng. Des.* 135 (2018) 346–355.
- [16] M.O. Vrieling, J. van Dommelen, M. Geers, Multi-scale fracture probability analysis of tungsten monoblocks under fusion conditions, *Nucl. Mater. Energy* 28 (2021) 101032.
- [17] V. Nikolic, S. Wurster, D. Firneis, R. Pippan, Improved fracture behavior and microstructural characterization of thin tungsten foils, *Nucl. Mater. Energy* 9 (2016) 181–188.
- [18] D. Scheiber, R. Pippan, P. Puschnig, L. Romaner, Ab initio calculations of grain boundaries in bcc metals, *Modelling Simul. Mater. Sci. Eng.* 24 (3) (2016) 035013.
- [19] S. Dorfman, V. Liubich, D. Fuks, K.C. Mundim, Simulations of decohesion and slip of the  $\Sigma 3(111)$  grain boundary in tungsten with non-empirically derived interatomic potentials: the influence of boron interstitials, *J. Phys.: Condens. Matter.* 13 (31) (2001) 6719.
- [20] J. Reiser, J. Hoffmann, U. Jäntsch, M. Klimenkov, S. Bonk, C. Bonnekoh, M. Rieth, A. Hoffmann, T. Mrotzek, Ductilisation of tungsten (W): On the shift of the brittle-to-ductile transition (BDT) to lower temperatures through cold rolling, *Int. J. Refract. Met. Hard Mater.* 54 (2016) 351–369.
- [21] M. Rieth, S.L. Dudarev, S.G. De Vicente, J. Aktaa, T. Ahlgren, S. Antusch, D. Armstrong, M. Balden, N. Baluc, M.-F. Barthe, et al., Recent progress in research on tungsten materials for nuclear fusion applications in Europe, *J. Nucl. Mater.* 432 (1–3) (2013) 482–500.
- [22] S. Hofmann, H. Hofmann, Influence of grain boundary segregation on mechanical properties of activated sintered tungsten, *J. Phys. Colloq.* 46 (C4) (1985) C4–633.
- [23] K. Povarova, A. Drachinskii, Y. Tolstobrov, Influence of microalloying on the cold brittleness temperature of tungsten, *Russ. Metall.* (1) (1987) 129–137.
- [24] J.R. Stephens, Effects of Interstitial Impurities on the Low-Temperature Tensile Properties of Tungsten, vol. 2287, National Aeronautics and Space Administration, 1964.
- [25] A. Joshi, D. Stein, Intergranular brittleness studies in tungsten using auger spectroscopy, *Metall. Trans.* 1 (1970) 2543–2546.
- [26] B.C. Muddle, D.V. Edmonds, Interfacial segregation and embrittlement in liquid phase sintered tungsten alloys, *Met. Sci.* 17 (4) (1983) 209–218.
- [27] J. Morniroli, M. Gantois, M. Lahaye, Brittle fracture of polycrystalline tungsten, *J. Mater. Sci.* 20 (1985) 199–206.
- [28] B. Gludovatz, S. Wurster, T. Weingärtner, A. Hoffmann, R. Pippan, Influence of impurities on the fracture behaviour of tungsten, *Phil. Mag.* 91 (22) (2011) 3006–3020.
- [29] D. Scheiber, R. Pippan, P. Puschnig, L. Romaner, Ab initio search for cohesion-enhancing impurity elements at grain boundaries in molybdenum and tungsten, *Modelling Simul. Mater. Sci. Eng.* 24 (8) (2016) 085009.
- [30] G.L. Krasko, Effect of impurities on the electronic structure of grain boundaries and intergranular cohesion in tungsten, *Int. J. Refract. Met. Hard Mater.* 12 (5) (1993) 251–260.
- [31] Z. Pan, L.J. Kecskes, Q. Wei, The nature behind the preferentially embrittling effect of impurities on the ductility of tungsten, *Comput. Mater. Sci.* 93 (2014) 104–111.
- [32] W. Setyawan, R.J. Kurtz, Effects of B, C, N, O, P and S Impurities on Tungsten  $\Sigma 27\{110\}\{552\}$  and  $\Sigma 3\{110\}\{112\}$  Grain Boundaries, vol. 53, Fusion Reactor Materials Program Report, Oak Ridge National Laboratory - MST Division, 2012, p. 64.
- [33] M. Grujicic, H. Zhao, G. Krasko, Atomistic simulation of  $\Sigma 3(111)$  grain boundary fracture in tungsten containing various impurities, *Int. J. Refract. Met. Hard Mater.* 15 (5–6) (1997) 341–355.
- [34] P.A.T. Olsson, P. Hiremath, S. Melin, Atomistic investigation of the impact of phosphorus impurities on the tungsten grain boundary decohesion, *Comput. Mater. Sci.* 219 (2023) 112017.
- [35] D.E. Spearot, K.I. Jacob, D.L. McDowell, Non-local separation constitutive laws for interfaces and their relation to nanoscale simulations, *Mech. Mater.* 36 (9) (2004) 825–847.
- [36] V. Yamakov, E. Saether, E. Glaesgen, Multiscale modeling of intergranular fracture in aluminum: constitutive relation for interface debonding, *J. Mater. Sci.* 43 (2008) 7488–7494.
- [37] W. Barrows, R. Dingreville, D. Spearot, Traction–separation relationships for hydrogen induced grain boundary embrittlement in nickel via molecular dynamics simulations, *Mater. Sci. Eng. A* 650 (2016) 354–364.
- [38] J.J. Möller, E. Bitzek, Fracture toughness and bond trapping of grain boundary cracks, *Acta Mater.* 73 (2014) 1–11.
- [39] P. Andric, W.A. Curtin, Atomistic modeling of fracture, *Modelling Simul. Mater. Sci. Eng.* 27 (1) (2018) 013001.
- [40] W.-S. Ko, J.B. Jeon, C.-H. Lee, J.-K. Lee, B.-J. Lee, Intergranular embrittlement of iron by phosphorus segregation: an atomistic simulation, *Modelling Simul. Mater. Sci. Eng.* 21 (2) (2013) 025012.
- [41] A.A. Griffith, VI. The phenomena of rupture and flow in solids, *Philos. Trans. R. Soc. Lond. Ser. A* 221 (582–593) (1921) 163–198.
- [42] S. Plimpton, Fast parallel algorithms for short-range molecular dynamics, *J. Comput. Phys.* 117 (1) (1995) 1–19, <http://dx.doi.org/10.1006/jcph.1995.1039>.
- [43] A.P. Thompson, H.M. Aktulga, R. Berger, D.S. Bolintineanu, W.M. Brown, P.S. Crozier, P.J. in 't Veld, A. Kohlmeyer, S.G. Moore, T.D. Nguyen, R. Shan, M.J. Stevens, J. Tranchida, C. Trott, S.J. Plimpton, LAMMPS - a flexible simulation tool for particle-based materials modeling at the atomic, meso, and continuum scales, *Comput. Phys. Comm.* 271 (2022) 108171.

- [44] B.-J. Lee, M.I. Baskes, Second nearest-neighbor modified embedded-atom-method potential, *Phys. Rev. B* 62 (2000) 8564–8567.
- [45] B.-J. Lee, M. Baskes, H. Kim, Y. Koo Cho, Second nearest-neighbor modified embedded atom method potentials for bcc transition metals, *Phys. Rev. B* 64 (2001) 184102.
- [46] M. Finnis, J. Sinclair, A simple empirical N-body potential for transition metals, *Phil. Mag. A* 50 (1) (1984) 45–55.
- [47] R. Hadian, B. Grabowski, J. Neugebauer, GBcode: A grain boundary generation code, *J. Open Source Softw.* 3 (29) (2018) 900.
- [48] D. Terentyev, X. He, A. Serra, J. Kuriplach, Structure and strength of  $\{110\}$  tilt grain boundaries in bcc Fe: An atomistic study, *Comput. Mater. Sci.* 49 (2) (2010) 419–429.
- [49] W. Setyawan, R.J. Kurtz, Effects of transition metals on the grain boundary cohesion in tungsten, *Scr. Mater.* 66 (8) (2012) 558–561.
- [50] D.C. Ghosh, R. Biswas, Theoretical calculation of absolute radii of atoms and ions. Part 1. The atomic radii, *Int. J. Mol. Sci.* 3 (2) (2002) 87–113.
- [51] M. Rahm, R. Hoffmann, N. Ashcroft, Atomic and ionic radii of elements 1–96, *Chem. Eur. J.* 22 (41) (2016) 14625–14632.
- [52] C. Bonnekoh, U. Jäntschi, J. Hoffmann, H. Leiste, A. Hartmaier, D. Weygand, A. Hoffmann, J. Reiser, The brittle-to-ductile transition in cold rolled tungsten plates: Impact of crystallographic texture, grain size and dislocation density on the transition temperature, *Int. J. Refract. Met. Hard Mater.* 78 (2019) 146–163.
- [53] B. Sadigh, P. Erhart, A. Stukowski, A. Caro, E. Martinez, L. Zepeda-Ruiz, Scalable parallel Monte Carlo algorithm for atomistic simulations of precipitation in alloys, *Phys. Rev. B* 85 (18) (2012) 184203.
- [54] N. Metropolis, A.W. Rosenbluth, M.N. Rosenbluth, A.H. Teller, E. Teller, Equation of state calculations by fast computing machines, *J. Chem. Phys.* 21 (6) (1953) 1087–1092.
- [55] G. Bhanot, The metropolis algorithm, *Rep. Progr. Phys.* 51 (3) (1988) 429.
- [56] P. Diaconis, L. Saloff-Coste, What do we know about the Metropolis algorithm? *J. Comput. System Sci.* 57 (1) (1998) 20–36.
- [57] I. Beichl, F. Sullivan, The metropolis algorithm, *Comput. Sci. Eng.* 2 (1) (2000) 65–69.
- [58] G.C. Sih, P. Paris, G. Irwin, On cracks in rectilinearly anisotropic bodies, *Int. J. Fract. Mech.* 1 (3) (1965) 189–203.
- [59] G.C. Sih, H. Liebowitz, Mathematical theories of brittle fracture, in: H. Liebowitz (Ed.), *Fracture: An Advanced Treatise*, in: *Mathematical Fundamentals*, vol. 2, Academic Press, NY, 1968, pp. 67–190, (Chapter 2).
- [60] P. Hiremath, S. Melin, E. Bitzek, P.A.T. Olsson, Effects of interatomic potential on fracture behaviour in single-and bicrystalline tungsten, *Comput. Mater. Sci.* 207 (2022) 111283.
- [61] P. Gumbsch, An atomistic study of brittle fracture: toward explicit failure criteria from atomistic modeling, *J. Mater. Res.* 10 (11) (1995) 2897–2907.
- [62] K.S. Cheung, S. Yip, A molecular-dynamics simulation of crack-tip extension: the brittle-to-ductile transition, *Modelling Simul. Mater. Sci. Eng.* 2 (4) (1994) 865.
- [63] E. Polak, G. Ribiere, Note sur la convergence de méthodes de directions conjuguées, *Rev. Fr. d'Inf. Rec. Oper. Ser. Rouge* 3 (16) (1969) 35–43.
- [64] O. Nguyen, M. Ortiz, Coarse-graining and renormalization of atomistic binding relations and universal macroscopic cohesive behavior, *J. Mech. Phys. Solids* 50 (8) (2002) 1727–1741.
- [65] P.A.T. Olsson, K. Kese, M. Kroon, A.M. Alvarez Holston, Ab initio-based fracture toughness estimates and transgranular traction-separation modelling of zirconium hydrides, *Modelling Simul. Mater. Sci. Eng.* 23 (4) (2015) 045015.
- [66] P.A.T. Olsson, M. Mrovec, M. Kroon, First principles characterisation of brittle transgranular fracture of titanium hydrides, *Acta Mater.* 118 (2016) 362–373.
- [67] G. Voronoi, Nouvelles applications des paramètres continus à la théorie des formes quadratiques, *J. Reine Angew. Math.* 133 (1907) 97–178.
- [68] C.H. Rycroft, VORO++: A three-dimensional Voronoi cell library in C++, *Chaos* 19 (4) (2009) 041111.
- [69] A. Stukowski, Visualization and analysis of atomistic simulation data with OVITO—the open visualization tool, *Modelling Simul. Mater. Sci. Eng.* 18 (1) (2009) 015012.
- [70] A. Stukowski, K. Albe, Extracting dislocations and non-dislocation crystal defects from atomistic simulation data, *Modelling Simul. Mater. Sci. Eng.* 18 (8) (2010) 085001.
- [71] A. Stukowski, Computational analysis methods in atomistic modeling of crystals, *JOM* 66 (2014) 399–407.
- [72] J.D. Honeycutt, H.C. Andersen, Molecular dynamics study of melting and freezing of small Lennard–Jones clusters, *J. Phys. Chem.* 91 (19) (1987) 4950–4963.